Article | Open Access

Energy Materials

Qie *et al. Energy Mater.* **2026**, *6*, 600092 **DOI:**10.20517/energymater.2026.137

Ni-doped CoTe with optimized *p*-band center for boosting polysulfide conversion kinetics in lithium-sulfur batteries

Jingjing Qie[1,#], Huiyue Sun[1,#], Shuang Geng[1,#], Yongqi Shang[1], Qunzhi Huang[1], Jishi Wei[1,2,*], Ke Chen[1], Taifeng Liu[3], Shuxi Dai[1,*], Wuxing Hua[1,4,*], Zhen Zhou[4]

Keywords:
Lithium-sulfur batteries, shuttle effect, Ni-doped CoTe, electronic structure

Citation: Qie, J.; Sun, H.; Geng, S.; Shang, Y.; Huang, Q.; Wei, J.; Chen, K.; Liu, T.; Dai, S.; Hua, W.; Zhou, Z. Ni-doped CoTe with optimized *p*-band center for boosting polysulfide conversion kinetics in lithium-sulfur batteries. *Energy Mater.* **2026**, *6*, 600092. https://dx.doi.org/10.20517/energymater.2026.137

Received: 27 May 2026 **First Decision:** 18 Jun 2026 **Revised:** 16 Jul 2026 **Accepted:** 23 Jul 2026 **Published:** 3 Aug 2026

Academic Editor: Wei Tang
Copy Editor: Ping Zhang
Production Editor: Ping Zhang

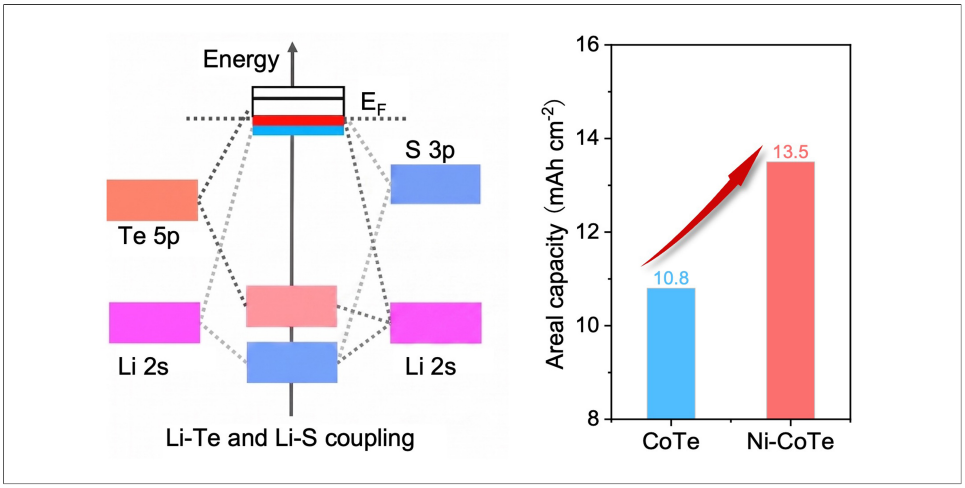

Abstract

Developing an effective electrocatalyst to regulate the kinetics of the sulfur redox reaction is essential for inhibiting polysulfide shuttling in Li-S batteries. Here, the electronic structure of CoTe, modulated by cation doping, is systematically investigated to elucidate how orbital hybridization optimizes sulfur redox electrocatalysis. Among the cation-doped CoTe compounds, the introduction of Ni dopants results in the most significant shift of the *p*-band center of CoTe (Ni-CoTe) towards the Fermi energy level, which facilitates the formation of numerous Te vacancies on the CoTe surface. This structural configuration endows CoTe with a multitude of active sites that bind polysulfide intermediates, lowering the activation energy (E_a) of the sulfur reduction reaction, specifically reducing the E_a for the conversion of lithium polysulfides to Li_2S from 0.73 eV to 0.65 eV. As a result, the Li-S

[1]Center for the Physics of Low-Dimensional Materials, Henan Joint International Research Laboratory of New Energy Materials and Devices, School of Physics and Electronics, Henan University, Kaifeng 475004, Henan, China.
[2]Henan Key Laboratory of Protection and Safety Energy Storage of Light Metal Materials, College of Chemistry and Molecular Sciences, Henan University, Kaifeng 475004, Henan, China.
[3]National & Local Joint Engineering Research Center for Applied Technology of Hybrid Nanomaterials, Henan University, Kaifeng 475004, Henan, China.
[4]College of New Energy and Intelligent Manufacturing, National Key Laboratory of Green Chemical Synthesis and Transformation Technology, Henan University, Zhengzhou 450046, Henan, China.
[#]These authors contributed equally to this work.

[*]**Correspondence to:** Prof. Jishi Wei, Prof. Shuxi Dai, Prof. Wuxing Hua, Center for the Physics of Low-Dimensional Materials, Henan Joint International Research Laboratory of New Energy Materials and Devices, School of Physics and Electronics, Henan University, Kaifeng 475004, Henan, China. E-mail: ecjsw@henu.edu.cn; shuxidai@henu.edu.cn; wxhua@henu.edu.cn

battery with Ni-CoTe catalyst delivers exceptional cyclability, with a low-capacity decay of 0.049% per cycle over 1,000 cycles at 2.0 C. Moreover, an initial areal capacity of 13.5 mAh cm^{-2} at 0.02 C is achieved with a high sulfur loading (10.0 mg cm^{-2}) and a low electrolyte-to-sulfur ratio (5.0 μL mg^{-1}). These findings will provide fundamental insights into orbital-level catalyst design principles for advanced sulfur electrochemistry.

INTRODUCTION

Lithium-sulfur (Li-S) batteries with high energy density (2,600 Wh kg^{-1}) and abundant sulfur resources are regarded as a highly promising option for future energy storage systems[1-3]. However, the intrinsically slow conversion kinetics from soluble intermediate lithium polysulfides (LiPSs, also denoted as Li_2S_n, $4 \leq n \leq 8$) to the charge/discharge products lead to the accumulation of LiPSs in organic electrolytes and their migration between electrodes under concentration gradients, commonly referred to as the "shuttle effect"[4-8]. This phenomenon is the main factor behind poor sulfur utilization and rapid capacity degradation, thus impeding the practical applications of Li-S batteries[9-11].

Extensive efforts have focused on addressing the challenges discussed above through strategies such as sulfur host design and separator modification[12-14]. However, these approaches are inherently passive, as they fail to effectively inhibit the dissolution and accumulation of LiPS[15,16]. In the consecutive sulfur reduction reaction (SRR) process, the increased activation energy required for the conversion from liquid LiPSs to solid discharge products results in the accumulation of LiPSs, thereby serving as the primary driver of the shuttle effect[17-19]. Therefore, the efficient electrocatalytic conversion of LiPSs is considered a proactive strategy for suppressing shuttle effects. Recently, a study on the *p*-charge descriptor as a predictor of SRR activity demonstrated that increasing the *p*-charge of p-block metal sulfides significantly optimized SRR kinetics[6]. This finding underscores the potential to enhance battery performance by designing heterogeneous catalysts with tailored *p*-band centers, which can be achieved through atom doping.

Two-dimensional transition metal tellurides (2D-TMTs), have garnered significant attention for their remarkable catalytic activity, particularly in terms of their adjustable *p*-band centers[20-22]. This has led to extensive research into their potential use as catalysts in Li-S batteries. For instance, cobalt telluride (CoTe) has been demonstrated to possess abundant catalytic active sites, enabling efficient capture of polysulfides and acceleration of their conversion[23,24]. However, the environmental susceptibility of TMTs, along with deficiencies in interactions with LiPSs, presents notable obstacles to their electrocatalytic performance, thereby constraining their application in Li-S batteries[20,25,26]. Cation-doping has demonstrated considerable promise in enhancing the catalytic activity of 2D transition metal chalcogenides through the augmentation of vacancies and the adjustment of the electronic structures, specifically the *p*-band centers[27,28].

EXPERIMENTAL

Materials

Carbon nanotube (99.9%) was purchased from Aladdin. $CoCl_2 \cdot 6H_2O$ (99%), $NiCl_2 \cdot 6H_2O$ (99%), $NaH_2PO_2 \cdot 2H_2O$ (99%), $Na_3C_6H_5O_7 \cdot 2H_2O$ (99%), and NaOH (98%) were purchased from InnoChem. Sulfur powder (99.5%) and ethanol (AR) were purchased from Kermel. Polyvinylidene fluoride (PVDF), polytetrafluoroethylene (PTFE), and the commercial membrane (Celgard 2500) were purchased from Canrd Technology Co. Ltd. Reduced graphene oxide (99.9%) was purchased from Carmery. The Li_2S_6 electrolyte (0.2 M) and Li_2S_8 electrolyte (0.2 M) were sourced from DODOCHEM. Deionized water was produced in-house.

Synthesis of Ni-Co

Nickel-cobalt (Ni-Co) nanosheets were synthesized via a typical hydrothermal method. In a standard procedure, $Na_3C_6H_5O_7·2H_2O$ (10 mmol), $CoCl_2·6H_2O$ (2 mmol), $NiCl_2·6H_2O$ (0.5 mmol), and $NaH_2PO_2·2H_2O$ (10 mmol) were dissolved in 80 mL of deionized water under magnetic stirring at 400 rpm and room temperature (~25 °C). The total time for complete dissolution is about 10 min. Subsequently, 10 mL of NaOH solution (10 M) was added dropwise, yielding final precursor concentrations of 22.22 mM Co^{2+} and 5.56 mM Ni^{2+}. After 10 min of stirring, the mixture was hydrothermally treated in a sealed 100 mL Teflon-lined autoclave at 150 °C for 24 h and then naturally cooled to room temperature. The resulting grey precipitate was collected by centrifugation, washed repeatedly with ethanol and deionized water, and dried under vacuum at 60 °C for 5 h. Co nanosheets were synthesized under identical conditions, but without adding $NiCl_2·6H_2O$.

Synthesis of Ni-CoTe and CoTe

Ni-CoTe was synthesized by placing Ni-Co and Te powder (in a mass ratio of 1:3) into separate quartz boats. The boats were positioned in the first and second temperature zones of a quartz tube furnace. A mixed gas of Ar/H_2 (volume ratio 9:1) was introduced into the tube. The tube was ramped to 200 °C at 5 °C·min^{-1} and subsequently annealed at this temperature for 4 h to yield Ni-CoTe. CoTe was prepared following the same procedure.

Preparation of Ni-CoTe interlayer

The Ni-CoTe interlayer was fabricated using a straightforward surface coating technique. Typically, a composite consisting of 70 wt.% Ni-CoTe, 20 wt.% Gr, and 10 wt.% PVDF was homogenized in N-methyl-2-pyrrolidone (NMP) via vigorous mechanical stirring to yield a well-dispersed slurry. The slurry was coated onto a clean Celgard 2500 separator and subsequently vacuum-dried at 55 °C for 8 h. After that, the separator was punched into 16-mm-diameter circular pieces. The areal loading of the interlayer was approximately 0.34 mg cm^{-2}. The CoTe and Gr interlayers were synthesized using the same method.

Synthesis of carbon nanotubes/sulfur cathodes

The carbon nanotubes/sulfur (CNTs/S) composite was synthesized using a simple melt-diffusion method. Specifically, CNTs and sulfur were combined in a mass ratio of 3:7, ground evenly, and then annealed at 155 °C for 12 h. The CNTs/S cathode was prepared by mixing CNTs/S, CNTs, and PVDF (8:1:1 w/w) in NMP. The resulting slurry was coated onto carbon-coated Al foil and vacuum-dried at 55 °C for 12 h.

Synthesis of freestanding high sulfur-loaded cathodes

The composite was obtained by mixing CNT/S, CNTs, and PTFE in ethanol, using a weight ratio of 80:15:5. The ethanol was subsequently evaporated using a dryer until the mixture achieved a consistency similar to silly putty. The resultant slurry was then rolled into a thin sheet and subsequently cut into 10 mm diameter circular electrodes. These electrodes were dried at 55 °C for 12 h.

Materials characterization

The composition of the products was analyzed using X-ray diffraction (XRD) (Bruker D8 ADVANCE, Bruker AXS GmbH, Germany) and Raman spectroscopy (LabRAM Odyssey, HORIBA France SAS, France). The chemical composition and valence states of the elements were examined by X-ray photoelectron spectroscopy (XPS) (SCIENTIFIC ESCALAB 250Xi, Thermo Fisher Scientific, USA). The microstructure and distribution of the materials were observed with a field emission scanning electron microscopy (SEM) (JSM-7001F, JEOL Ltd., Japan). Transmission electron microscopy (FEI Tecnai G2 F20, FEI Company, USA) was used to further observe nanoscale size, shape, and structure, as well as any potential crystal defects. Electron paramagnetic resonance (Bruker EMX PLUS, Bruker BioSpin GmbH, Germany) spectroscopy was

employed to detect the formation of Te vacancies, with the magnetic field set between 2,000 and 5,000 G and a scan rate of 10 G s^{-1}.

Electrochemical measurements

Battery fabrication was carried out inside an argon-purged glove box, employing a conventional Li-S electrolyte solution and Li foil as the counter electrode. The battery performance was characterized by galvanostatic cycling with the Neware test system (Neware Technology Limited, China) within the voltage range of 1.7-2.7 V, by cyclic voltammetry (CV) with the Ivium workstation (Ivium Technologies B.V., Netherlands), and by electrochemical impedance spectroscopy (EIS) with the DH7000C workstation (Jiangsu Donghua Analytical Instrument Co., Ltd., China) over a frequency range of 0.1 Hz to 10^4 Hz.

H-type glass cells penetration experiment and Li_2S_6 adsorption test

An H-type glass cell (5 mL) was employed to evaluate the polysulfide blocking capability of different modified separators. The cell consisted of two chambers separated by the modified separator. The left chamber was filled with a 20 mM Li_2S_6 solution (in LiTFSI electrolyte), while the right chamber contained pure LiTFSI electrolyte without polysulfides. The color change or concentration variation of the solution in the right chamber was monitored after different standing durations inside an argon-filled glovebox.

The adsorption capability of the different modified separators for polysulfides was further characterized using ultraviolet-visible (UV-vis) absorption spectroscopy. The UV-vis spectra were recorded to analyze the absorption intensity of the Li_2S_6 solution before and after adsorption, enabling quantitative evaluation of polysulfide removal efficiency.

Measurement for the deposition of Li_2S

The battery was constructed with Ni-CoTe or CoTe composites deposited onto 10-mm-diameter carbon paper as the cathode and Li foil as the anode. 20 μL of 0.2 M Li_2S_8 solution was used as the catholyte, and 20 μL of conventional Li-S electrolyte was used as the anolyte. The assembled cells were discharged via a galvanostatic step at 0.112 mA until the voltage decreased to 2.06 V, and then held potentiostatically at 2.05 V for Li_2S deposition until the current dropped to 10^{-5} A.

In situ Raman spectroscopy

A Li-S battery incorporating a quartz window for *in situ* Raman spectroscopy analysis at a 532 nm laser wavelength was assembled using Ni-CoTe or CoTe as the interlayer. The battery was evaluated at 0.2 C.

Density functional theory calculations

All density functional theory (DFT) computations were carried out with the Vienna Ab-initio Simulation Package (VASP) code, while the exchange-correlation functional was described via the generalized gradient approximation (GGA) using the Perdew-Burke-Ernzerhof (PBE) parametrization. The (103) crystal surface of CoTe was selected for its low surface energy and structural stability. The surface slab was constructed comprising 24 Co and 24 Te atoms, using the optimized bulk lattice constants. A vacuum layer of 15 Å was applied along the surface-normal direction to eliminate periodic interactions. Structural relaxations were performed using a 2 × 2 × 1 Monkhorst-Pack k-point mesh and a 300 eV plane-wave cutoff. Convergence thresholds were set to 10^{-5} eV for total energy and 0.01 eV $Å^{-1}$ for the maximum atomic force.

The adsorption energy ΔE_{ad} was calculated as[29]:

$$\Delta E_{ad} = E_{(surf+ad)} - E_{surf} - E_{ad} \quad (1)$$

In which the symbols $E_{(surf+ad)}$, $E_{surf,}$ and E_{ad} denote the energies of the LiPS-adsorbed surface, the clean substrate, and the free LiPSs, respectively.

The Gibbs free energy is evaluated via the following equation[29]:

$$\Delta G\ (S_8 - Li_2S_8) : E_{(Li_2S_8)} - E_{S_8} - 2E_{(Li^+)} \quad (2)$$

$$\Delta G\ (Li_2S_8 - Li_2S_6) : E_{(Li_2S_6)} - E_{Li_2S_8} + 0.25E_{S_8} \quad (3)$$

$$\Delta G\ (Li_2S_6 - Li_2S_4) : E_{(Li_2S_4)} - E_{Li_2S_6} + 0.25E_{S_8} \quad (4)$$

$$\Delta G\ (Li_2S_4 - Li_2S_2) : E_{(Li_2S_2)} - E_{Li_2S_4} + 0.25E_{S_8} \quad (5)$$

$$\Delta G\ (Li_2S_2 - Li_2S) : E_{(Li_2S)} - E_{Li_2S_2} + 0.25E_{S_8} \quad (6)$$

RESULTS AND DISCUSSION

Theoretical analyses and structural modulations for catalyst design

Interfacial interactions involving surface adsorption and charge transfer in Li-S batteries critically impact the sulfur conversion process[30,31]. Thus, regulating interfacial interactions at the substrate surface is essential for sulfur redox reactions[32,33]. In analogy to the *d*-band center theory for metals, the *p*-band center of nonmetallic anions is a key descriptor that significantly influences the adsorption energy of reaction intermediates, similar to how the *d*-band center affects proton adsorption in electrocatalysis[29,34].

To investigate the relationship between the Te *p*-band electronic structure and sulfur redox kinetics, a series of M-CoTe (M= V, Mn, Fe, Ni, Cu, Zn) compounds were designed to regulate the Te electronic structure. The calculated projected density of states (PDOS) in Figure 1A shows that the Te *p*-band center exhibits the most significant upward shift toward the Fermi energy level (E_F) upon Ni doping, which strengthens interfacial electronic interactions by modulating the Li-Te orbital coupling, thereby optimizing the adsorption strength between M-CoTe and LiPSs. Simultaneously, the *d*-band center of the Co site shifts toward the E_F upon Ni doping, from -2.937 eV in pure CoTe to -2.858 eV in Ni-CoTe, which tunes the occupancy of the antibonding orbitals between Co and LiPSs, adjusting the adsorption strength to an optimal level [Supplementary Figure 1]. The strategy of concurrently regulating Co *d*-band and Te *p*-band through Ni doping prevents excessive binding of reaction intermediates, thus preserving the availability of active catalytic sites[35]. Furthermore, the adsorption configurations of $^*S_8$ and Li_2S_x (x = 1, 2, 4, 6, 8) on Ni-CoTe suggest that the Co, Ni, and Te sites form Co-S, Ni-S, and Li-Te bonds with the S and Li atoms in the polysulfides, whereas only Co-S and Li-Te bonds are observed on the CoTe catalyst [Supplementary Figures 2 and 3]. The adsorption energies of $^*S_8$, $^*Li_2S_8$, $^*Li_2S_6$, $^*Li_2S_4$, $^*Li_2S_2$, and $^*Li_2S$ on the Ni-CoTe surface are -0.95, -1.54, -1.49, -1.84, -2.08, and -3.01 eV, respectively, which are higher than those on the CoTe surface [Figure 1B]. The enhanced adsorption of LiPSs on Ni-CoTe significantly optimized the sulfur redox kinetics.

Materials characterization

Ni-CoTe nanosheets were synthesized through a hydrothermal method, followed by a chemical vapor deposition (CVD) step, with detailed preparation protocols provided in Supplementary Figure 4. For comparative purposes, CoTe and V-CoTe nanosheets were synthesized using the same procedure. SEM images reveal that the initial Ni-Co nanosheets exhibit a hexagonal structure [Supplementary Figure 5]. Subsequent SEM analyses [Figure 2A] confirm that the nanosheets retain their hexagonal morphology after the CVD treatment. The high-resolution TEM (HRTEM) image of Ni-CoTe [Figure 2B] and its inverse fast-Fourier-transform (IFFT) pattern [Figure 2C] present a clear crystalline structure, with a lattice spacing of

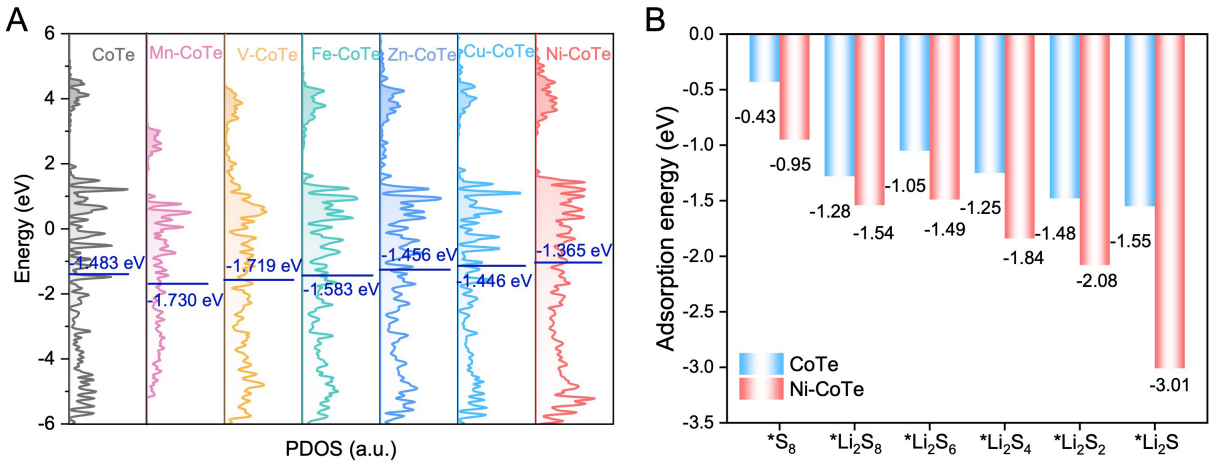

Figure 1. (A) *p*-band center of M-CoTe relative to the Fermi level; (B) Adsorption energy for $*Li_2S_x$ (x = 1, 2, 4, 6, 8) and $*S_8$ on the Ni-CoTe and CoTe catalyst. PDOS: Projected density of states.

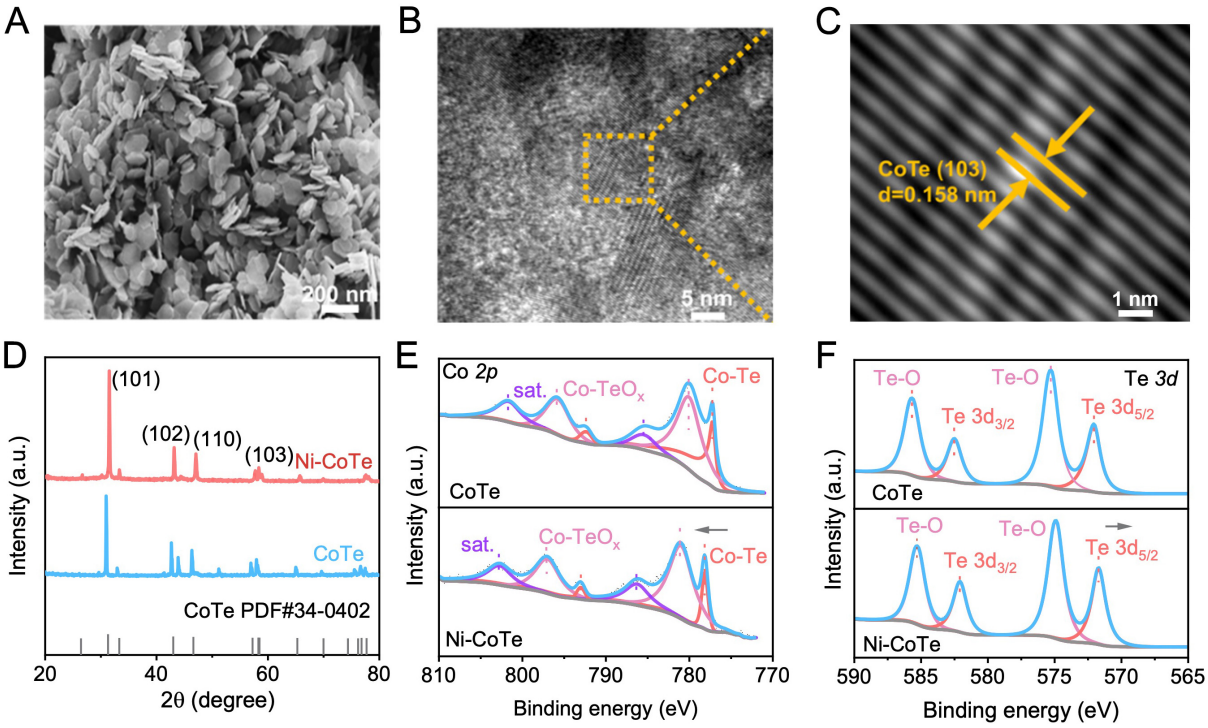

Figure 2. (A) Scanning electron microscopy (SEM) image of the Ni-CoTe catalyst; (B) High-resolution transmission electron microscopy (HRTEM); (C) Inverse fast Fourier-transform (IFFT) lattice images of Ni-CoTe; (D) X-ray diffraction (XRD) patterns of CoTe and Ni-CoTe; (E) X-ray photoelectron spectroscopy (XPS) spectra of Co 2*p* and (F) Te 3*d* for the Ni-CoTe and CoTe catalysts.

0.158 nm corresponding to the (103) facet of CoTe. XRD confirmed the successful synthesis and crystal phase of the as-prepared Ni-CoTe. As shown in Figure 2D, the predominant signals match well with the characteristic peaks of CoTe (PDF#34-0402), consistent with the HRTEM results. The clear diffraction peaks indicate good crystallinity, with peaks at 31.3°, 42.3°, 46.6°, and 58.2° corresponding to the (101), (102), (110), and (103) planes of orthorhombic CoTe. It is worth noting that introducing a small amount of Ni into CoTe slightly shifted the main XRD peak without creating new phases, indicating successful intercalation into the crystal lattice[36].

XPS was then employed to analyze the composition, elemental valence states, and electron transfer in Ni-CoTe [Figure 2E and F, Supplementary Figure 6]. The Ni-CoTe spectra exhibit Co *2p* peaks that are shifted by +0.8 eV to higher binding energy in comparison to those in CoTe, while the Te *3d* spectra demonstrate a slight downshift of -0.4 eV to lower binding energy. These alterations in binding energy indicate substantial electronic coupling between Ni and CoTe, suggesting electron transfer from Ni to Te and modifying the electronic structure of CoTe, further corroborating the successful incorporation of Ni into CoTe[37]. Furthermore, in contrast to the flat Electron paramagnetic resonance (EPR) signal observed in CoTe, the Ni-CoTe sample exhibited an unpaired-electron peak with a g-value of 2.000, attributed to the removal of Te atoms [Supplementary Figure 7][38]. The enhanced signal intensity in Ni-CoTe indicates a higher concentration of unpaired electrons, confirming the introduction of Te vacancies induced by Ni doping. This result also suggests possible electron transfer between the defect sites and metal centers in Ni-CoTe, which plays a key role in boosting the catalytic activity for optimizing sulfur redox kinetics.

Catalytic activity

Li-S batteries were assembled using CNTs/S cathodes and different interlayers [Ni-CoTe, V-CoTe, or CoTe-modified polypropylene (PP) separators] with lithium foil as the reference anode. The rate performance of the three batteries was systematically compared [Supplementary Figure 8]. The Ni-CoTe battery consistently achieved the highest capacities at all rates and displayed a reduced overpotential (ΔE = 151.5 mV) compared with the V-CoTe (177.9 mV) and CoTe (173.6 mV) batteries. This experimental trend corroborates the theoretical prediction that the doping of Ni causes Te *p*-band center to exhibit the most significant upward shift, which significantly optimizes the sulfur redox kinetics. Based on the theoretical calculations and electrochemical results, this study investigates the catalytic activity of Ni-CoTe for sulfur redox electrocatalysis in the subsequent discussion.

The catalytic activity of the as-prepared Ni-CoTe nanosheets was evaluated by performing three consecutive CV measurements on the Ni-CoTe, CoTe, and Gr electrodes [Supplementary Figure 9]. The nearly identical CV plots for the three batteries indicate reversible electrochemical properties. Figure 3A shows the first-cycle CV plots for the three batteries. In the SRR process, two cathodic peaks at ≈2.30 V (C_1) and 2.05 V (C_2) indicate the conversion of S_8 to soluble Li_2S_n and then to Li_2S. During the sulfur evolution reaction, two anodic peaks at ≈2.30 V (A_1) and 2.36 V (A_2) correspond to the conversion of Li_2S back to Li_2S_n, and finally to S_8. Notably, the Ni-CoTe battery exhibited the highest current response and largest peak areas for both cathodic and anodic peaks, suggesting enhanced electrochemical reaction kinetics[39]. This enhancement is attributed to Ni doping-induced Te vacancies and the regulation of the *p*-band center of CoTe.

Tafel slopes obtained from CV curves were further fitted to confirm the high electrocatalytic activity of the Ni-CoTe catalysts [Figure 3B and Supplementary Figure 10]. The Ni-CoTe battery exhibited a lower Tafel slope than the CoTe and Gr batteries in both the reduction ($Li_2S_n \rightarrow Li_2S$) and the oxidation ($Li_2S \rightarrow$ soluble Li_2S_n) processes. To evaluate the reproducibility and reliability of the Tafel slope analysis, the average Tafel slopes from the three cycles are shown in Figure 3C alongside the cycle-to-cycle variation represented by error bars. The less-than-4% bias indicated by these bars confirms the strong reliability of the measured data. The reduction in Tafel slopes observed for both the oxidation and reduction processes in the Ni-CoTe battery confirms its bidirectional catalytic capability toward LiPS conversion[40,41].

Li_2S precipitation/dissolution tests were further employed to assess the liquid-solid and solid-liquid conversion efficiency facilitated by the Ni-CoTe catalyst[42]. Coin cells were assembled utilizing CP@Ni-CoTe, CP@CoTe, and CP@Gr (where Ni-CoTe nanosheets, CoTe nanosheets, or graphene were loaded onto carbon fiber paper, respectively denoted as CP@Ni-CoTe, CP@CoTe, and CP@Gr) as cathodes, lithium foil as the anode, and a Li_2S_8/tetraglyme solution as the catholyte. The Li_2S precipitation capacity was

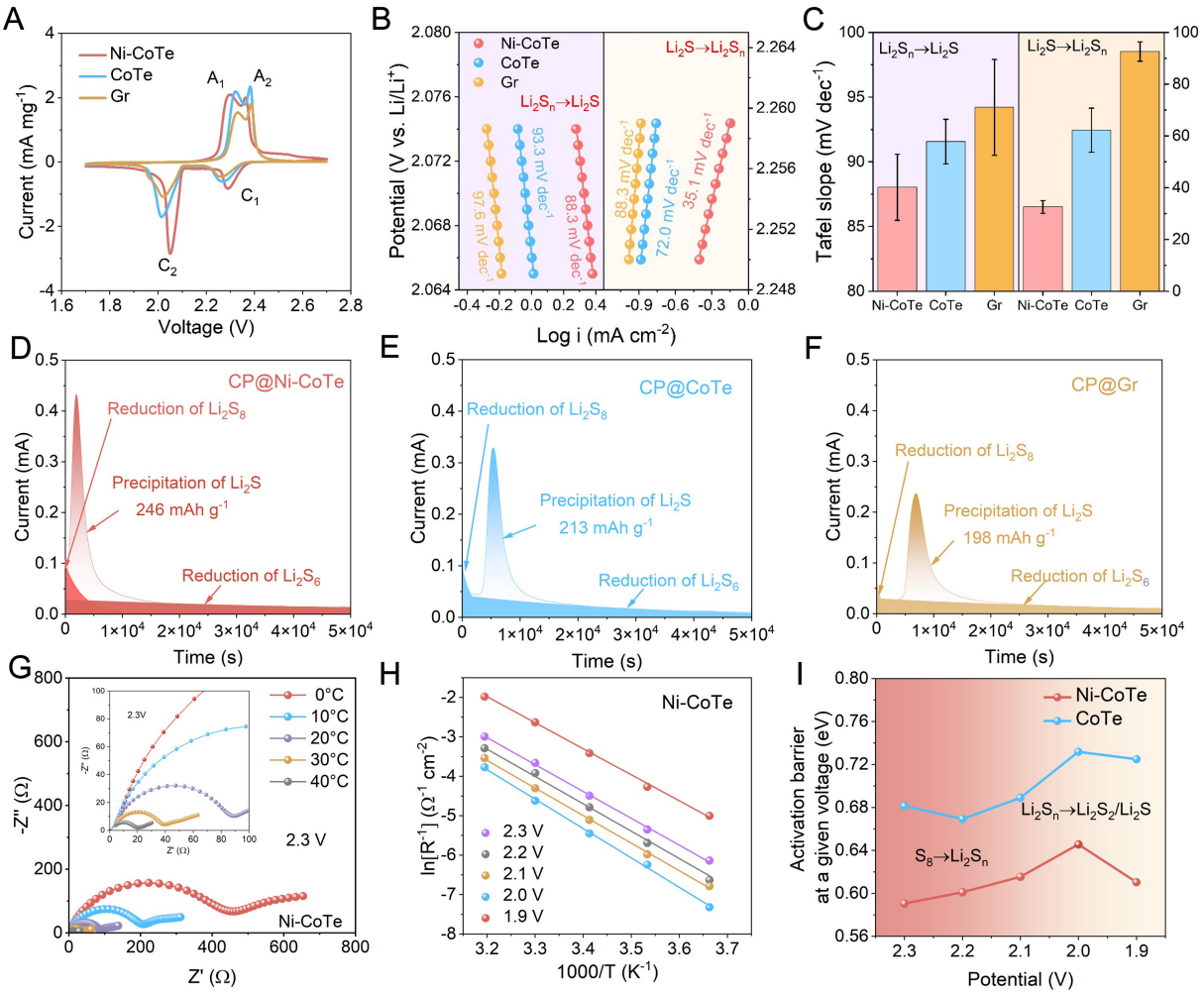

Figure 3. (A) The first cycle of CV profiles for batteries with different catalysts at a scan rate of 0.1 mV s^{-1}; (B) Tafel slopes derived from the CV profiles in (A); (C) Tafel slopes of Ni-CoTe, CoTe, and Gr derived from three CV cycles. The error bars represent the standard deviation (cycle-to-cycle variation) of the Tafel slopes calculated from three consecutive CV cycles; (D-F) Potentiostatic discharge profiles at 2.05 V; (G) Temperature-dependent EIS spectra of the Ni-CoTe cell at 2.3 V; (H) Corresponding Arrhenius plots derived from (G); (I) Discharge activation barriers of Ni-CoTe and CoTe cells calculated from (H). EIS: Electrochemical impedance spectroscopy; CV: cyclic voltammetry.

quantitatively determined based on Faraday's law [Supplementary Figure 11]. As shown in Figure 3D-F and Supplementary Figure 12, the CP@Ni-CoTe cathode demonstrated the highest capacity of 246 mAh g^{-1} and the earliest nucleation time (1947 s). Furthermore, in contrast to the pronounced Li_2S aggregation observed on the CP@CoTe and CP@Gr electrodes, SEM images in Supplementary Figure 13 show a uniform Li_2S deposition on the CP@Ni-CoTe electrode. This finding provides direct evidence for the accelerated conversion of LiPSs to Li_2S enhanced by the Ni-CoTe catalyst[17]. Additionally, the CP@Ni-CoTe electrode demonstrated the highest Li_2S dissolution capacity and the earliest onset of Li_2S dissolution, relative to those of the CP@CoTe and CP@Gr electrodes [Supplementary Figure 14]. These results confirm that the Ni-CoTe nanosheets function as bidirectional catalysts, accelerating both the reduction of LiPSs and the oxidation of Li_2S[43].

The SRR kinetics (E_a) at a given voltage were experimentally determined by fitting the charge transfer resistance (R_{ct}), measured at different temperatures using EIS, to the Arrhenius equation [Figure 3G and H, Supplementary Figures 15-17][44,45]. To ensure voltage stability during the specified redox reaction, the battery was initially discharged to a preset potential and subsequently maintained at that level via

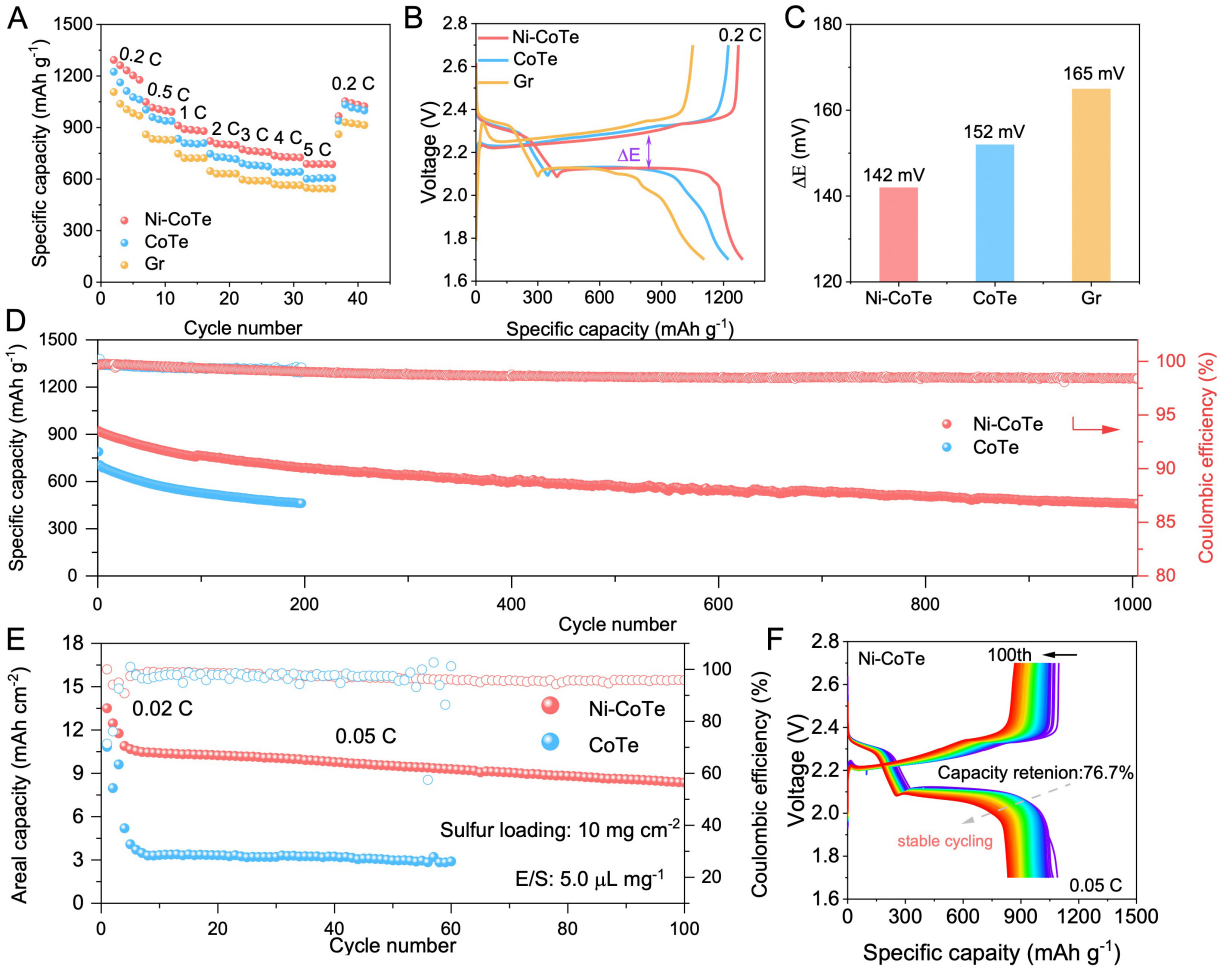

Figure 4. (A) Rate performance; (B) Initial charge-discharge curves of the three batteries at 0.2 C; (C) Plateau-voltage-derived overpotentials at 0.2 C; (D) Cycling performance at 2.0 C; (E) Cycling performance of Ni-CoTe and CoTe batteries with high sulfur loadings; (F) Charge-discharge profiles of the Ni-CoTe battery over 100 cycles at 0.05 C.

chronoamperometric control. Following this, EIS measurements were carried out across a range of temperatures, with the thermal environment precisely controlled by a variable-temperature thermotank. As shown in Figure 3I, the Ni-CoTe battery exhibited a lower E_a of 0.59 eV, in contrast to the CoTe battery (0.68 eV), suggesting a more efficient conversion of S_8 to Li_2S_n facilitated by the Ni-CoTe catalyst[44]. When the voltage decreased to 2.0 V, corresponding to the conversion of RDS (Li_2S_n to Li_2S_2/Li_2S), the E_a for the Ni-CoTe battery increased marginally to 0.65 eV. However, the CoTe battery demonstrated a higher E_a of 0.73 eV at this voltage, resulting in the accumulation of LiPSs and thus the shuttle effect, ultimately diminishing sulfur utilization. The substantial reduction in E_a of RDS, facilitated by the Ni-CoTe catalyst, significantly mitigates the accumulation of Li_2S_n and their diffusion to the lithium anode.

Electrochemical performances

The rate performance of Li-S batteries was compared at rates ranging from 0.2 to 5.0 C (1 C = 1,675 mA g^{-1}) to evaluate the sulfur redox chemistry [Figure 4A] under conditions of an areal sulfur loading of ~1.0 mg cm^{-2} and 20 μL of electrolyte on the cathode side. The Ni-CoTe battery delivered a significantly higher initial capacity of 1,293.2 mAh g^{-1} compared to the CoTe (1,224.0 mAh g^{-1}) and the Gr (1,106.5 mAh g^{-1}) batteries. Upon increasing the rate to 0.5, 1.0, 2.0, 3.0, 4.0, and 5.0 C, the Ni-CoTe battery respectively demonstrated elevated capacities of 1,048.6, 911.3, 821.5, 773.1, 735.9, and 688.0 mAh g^{-1}, much higher than those of other batteries, suggesting efficient utilization of active sulfur even at high current density[46,47].

The overpotential (ΔE) of the Ni-CoTe battery, calculated from the first-cycle charge/discharge plateaus, was 142 mV, notably lower than the values for the CoTe (152 mV) and Gr (165 mV) batteries [Figure 4B and C]. Furthermore, the differential plots corresponding to the charge/discharge profiles of Ni-CoTe, CoTe, and Gr batteries have been analyzed [Supplementary Figure 18], further revealing that the Ni-CoTe battery exhibits a lower overpotential compared to the CoTe battery and the Gr battery. The lower overpotential suggests that the electrochemical kinetics are more favorable with the Ni-CoTe catalyst[48]. Besides, the shuttle constant (k_s) obtained from the charge/discharge profiles is much lower for the Ni-CoTe battery (0.054 h^{-1}) than that for the CoTe (0.070 h^{-1}) and Gr (0.126 h^{-1}) batteries [Supplementary Figures 19 and 20], which indicates that the shuttle effect was effectively inhibited with the Ni-CoTe catalyst, enhancing the utilization of sulfur[6].

To directly assess the impact of catalysis on battery lifespan, cycling performance at 2.0 C was compared. As shown in Figure 4D, the Ni-CoTe battery achieved a high initial specific capacity of 921.9 mAh g^{-1} at 2.0 C, with capacity retention reflected in a low decay rate of 0.049 % per cycle over 1,000 cycles. Notably, this long-term stability test was conducted under conditions of low-sulfur loading (0.88 mg cm^{-2}) and excess electrolyte (20 μL on the cathode side), which were intentionally chosen to evaluate the intrinsic catalytic activity of the Ni-CoTe catalyst. In sharp contrast, the CoTe battery suffered from rapid capacity fading, declining to 461.8 mAh g^{-1} with a decay rate of 0.21% per cycle after 200 cycles. Furthermore, the Ni-CoTe battery exhibited more stable Coulombic efficiency than the CoTe battery, indicating that polysulfide shuttling was significantly suppressed. It is widely considered that both the increase in areal sulfur loading and the decrease in electrolyte dosage are essential for the prospective application of Li-S batteries. Therefore, batteries with a sulfur loading as high as 10.0 mg cm^{-2} and an E/S ratio of only 5.0 μL mg^{-1} were constructed. As shown in Figure 4E, with an initial capacity of 1,350.5 mAh g^{-1} (13.5 mAh cm^{-2}) at 0.02 C, the Ni-CoTe battery also showed a high areal capacity of 10.9 mAh cm^{-2} when tested at 0.05 C. Moreover, a capacity of 8.36 mAh cm^{-2} was maintained over 100 cycles, affording a retention of 76.7%; the initial capacity and its retention capability at 0.05 C were much superior to those of the CoTe battery, indicating improved sulfur utilization with the Ni-CoTe catalyst. The electrochemical performance surpassed most high-sulfur-loaded Li-S batteries reported in previous literature [Supplementary Table 1], demonstrating promising prospects for practical application[40,48-56]. Furthermore, compared with the CoTe battery, the Ni-CoTe battery exhibited stable discharge-charge plateaus and Coulombic efficiency during cycling under such a high sulfur mass loading, confirming the high catalytic activity of the Ni-CoTe catalyst in promoting polysulfide conversion [Figure 4E and F, Supplementary Figure 21].

The inhibition of polysulfide shuttling

To further verify that the shuttle effect was inhibited with the Ni-CoTe catalyst, an *in situ* Raman test was performed during cycling at 0.2 C. A Li-S battery was assembled using a polypropylene separator modified with Ni-CoTe or CoTe catalyst, a quartz window, and a small aperture in the lithium anode, allowing confocal Raman signals to be captured at the separator/lithium interfaces [Figure 5A-F][57,58]. When using the CoTe-modified separator, characteristic Raman peaks at 218 and 472 cm^{-1}, assigned to S_8^{2-}, were observed around 2.5 V, indicating the liberation and migration of high-order LiPSs from the conductive substrate toward the lithium anode[48]. As discharge proceeded, the S_8^{2-} peaks diminished, while peaks at 398 and 534 cm^{-1} corresponding to Li_2S_6/Li_2S_4 and Li_2S_3 were detected at 2.2 V, indicating the conversion from long-chain LiPSs to short-chain LiPSs. At the end of the discharge, the disappearance of these LiPS peaks suggested further reduction to Li_2S_2/Li_2S, either on the anode or upon returning to the cathode, leading to reduced sulfur utilization and a consequent decline in discharge capacity[59]. Upon charging, the S_6^{2-}/S_4^{2-} and S_3^{2-} peaks were redetected, indicating substantial shuttling of soluble LiPSs. In sharp contrast, when the Ni-CoTe-modified separator was employed, the observed Raman spectra showed distinct differences. Only small LiPS signals were detected in the Ni-CoTe battery during both discharge and charge processes [Figure 5D-F], indicating effective suppression of polysulfide shuttling during cycling.

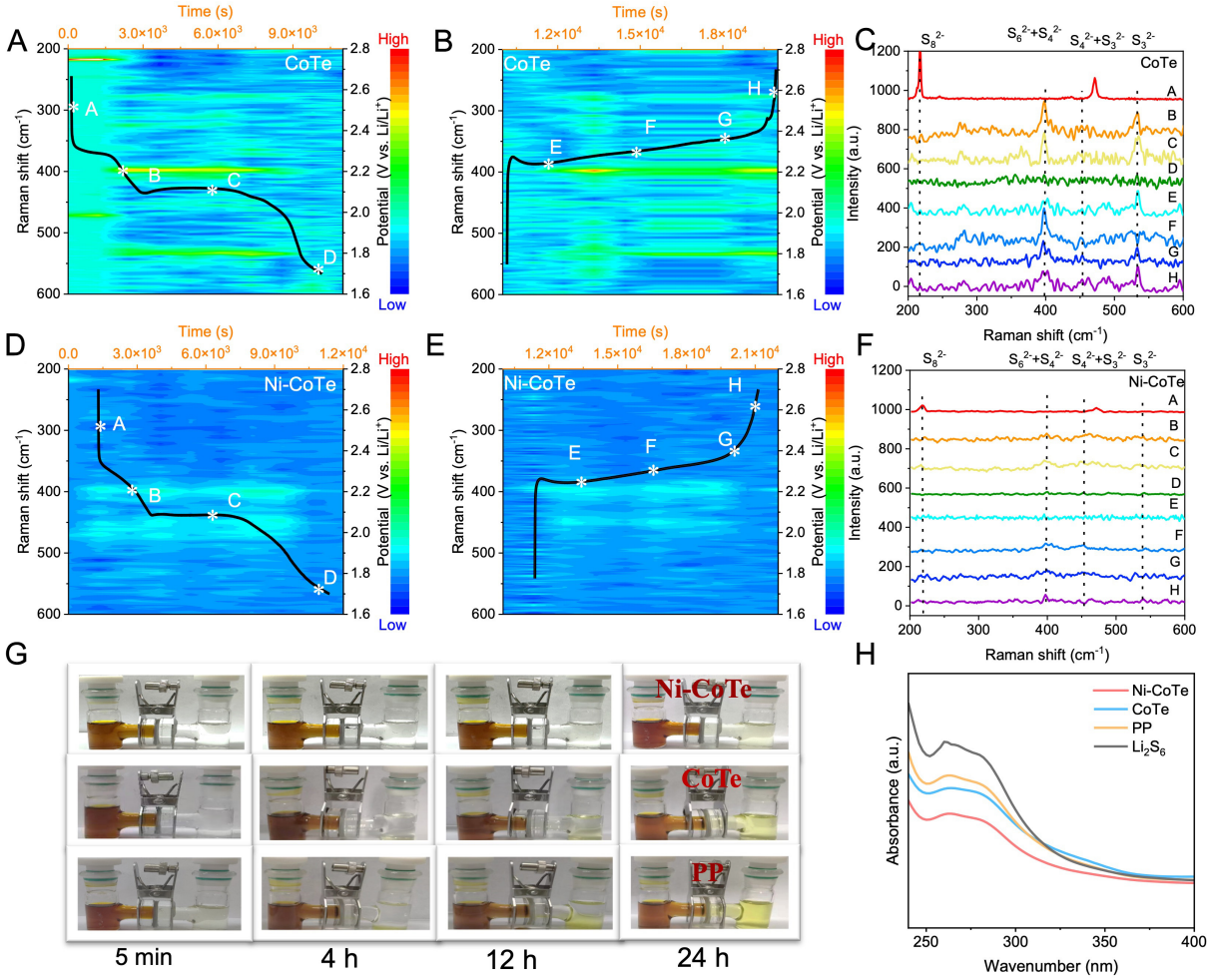

Figure 5. Time-resolved Raman spectra of Li-S batteries during discharge and charge at 0.2 C, with (A-C) CoTe and (D-F) Ni-CoTe coated separators. The black curves on the contour maps show the galvanostatic voltage profiles, with white stars A-H indicating the electrochemical states for the representative Raman spectra. (A-D)and (E-H) denote selected states during discharge and charge, respectively. The corresponding Raman spectra for states A-H are presented in (C) for the CoTe battery and in (F) for the Ni-CoTe battery; (G) Polysulfide permeation in H-type cells using Ni-CoTe-coated, CoTe-coated, and uncoated PP separators; (H) UV-vis spectra of the blank-side electrolytes after 24 h for the three configurations. UV-vis: Ultraviolet-visible.

To further investigate suppression of polysulfide shuttling, H-shaped electrolytic cells were assembled, with Ni-CoTe-coated, CoTe-coated, and uncoated separators positioned between two electrolytes. As shown in Figure 5G-H, the left chamber contained 5 mL of 20 mM Li_2S_6 solution, while the right chamber held 5 mL of blank electrolyte, and the two compartments were separated by either a Ni-CoTe-coated, CoTe-coated, or uncoated separator. Experiments conducted with uncoated separators revealed significant Li_2S_6 permeation within 4 h, whereas both the Ni-CoTe and CoTe separators kept the right chamber colorless. After 12 h of standing, the uncoated separator caused the solution in the right chamber to turn yellow. In contrast, the CoTe separator allowed only a limited amount of Li_2S_6 to cross over this period, resulting in a faint yellow, while the Ni-CoTe separator maintained the right chamber almost colorless. This result indicates that both CoTe and Ni-CoTe coatings significantly suppress LiPS permeation compared to the uncoated PP separator, with Ni-CoTe providing substantially superior suppression. Extending the standing time to 24 h resulted in nearly identical coloration on both sides of the cell with an uncoated PP separator, while the CoTe-coated separator gave rise to a light yellow in the right chamber. By sharp contrast, the right chamber exhibited a considerably paler shade when the Ni-CoTe separator was employed. The Li_2S_6 concentration in the right-chamber electrolyte was monitored via ultraviolet-visible (UV/Vis) spectroscopy. As shown in Figure 5H,

after 24 h, the S_6^{2-} peak intensity at 265 nm for the solution exposed to the Ni-CoTe separator was lower than that for the solution exposed to the CoTe separator and the uncoated PP separator. These results confirm that Ni-CoTe possesses a strong adsorption capacity for LiPSs, thereby effectively suppressing the polysulfide shuttling.

Recently, novel electrolytes such as sparingly solvating electrolytes (SSEs) have shown great promise in preventing polysulfide shuttling but faced challenges in catalyzing sulfur conversion[60]. The Ni-CoTe catalyst, with its abundant Te vacancies and optimized *p*-band center, provided strong adsorption sites that facilitate the direct capture and subsequent conversion of LiPSs at the catalyst surface. Therefore, the combined effect of SSEs and Ni-CoTe is anticipated to significantly improve battery performance, particularly under practical conditions of high sulfur loading and lean electrolyte.

CONCLUSION

In summary, we have successfully designed and synthesized a Ni-CoTe electrocatalyst to optimize the sulfur redox kinetics for inhibiting polysulfide shuttling. Experimental and theoretical results consistently showed that Ni doping introduced Te vacancies, which elevated the *p*-band center. This enhancement strengthened the chemical interaction with LiPSs, reducing the activation energy of the RDS for the SRR from 0.73 eV to 0.65 eV and promoting Li_2S nucleation. Consequently, the Ni-CoTe battery demonstrated durable cycling performance at 2.0 C for 1,000 cycles, corresponding to a decay rate as low as 0.049% per cycle. Moreover, under the conditions of 10.0 mg cm^{-2} sulfur and E/S of 5.0 μL mg^{-1}, the Ni-CoTe battery delivered an areal capacity of 8.36 mAh cm^{-2} upon 100 cycles at 0.05 C. This work demonstrates an electronic structure regulation strategy to enhance the catalytic activity of transition-metal tellurides for high-performance Li-S batteries.

DECLARATIONS

Authors' contributions

Contributed equally to this work: Qie, J.; Sun, H.; Geng, S.
Designed the research, supervised experiments, and edited the paper: Wei, J.; Dai, S.; Chen, K.; Hua, W.; Zhou, Z.
Carried out the experiments, analyzed the electrochemical data and wrote the paper: Qie, J.; Sun, H.
Contributed to the DFT calculations and discussion on the electronic properties of the catalysts: Geng, S.; Liu, T.
Characterized the materials and analyzed the results: Qie, J.; Sun, H.; Geng, S.; Shang, Y.; Huang, Q.
All authors discussed the results and commented on the paper.

Availability of data and materials

The data supporting the findings of this study are available within this Article and its Supplementary Materials. Further data are available from the corresponding authors upon request.

AI and AI-assisted tools statement

Not applicable.

Financial support and sponsorship

This work was financially supported by the National Natural Science Foundation of China (Nos. 22309042, 22579046, 52272038, 22308086), the Natural Science Foundation of Henan (262300421041), and Program for Science and Technology Innovation Talents in University of Henan Province (26HASTIT003).

Conflicts of interest

All authors declared that there are no conflicts of interest.

Ethical approval and consent to participate

Not applicable.

Consent for Publication

Not applicable.

Supplementary Materials

Supplementary Materials

REFERENCES

1. Zhou, S.; Shi, J.; Liu, S.; et al. Visualizing interfacial collective reaction behaviour of Li-S batteries. *Nature* **2023**, *621*, 75-81. DOI
2. Manthiram, A.; Chung, S. H.; Zu, C. Lithium-sulfur batteries: progress and prospects. *Adv. Mater.* **2015**, *27*, 1980-2006. DOI PubMed
3. Zhou, T.; Lv, W.; Li, J.; et al. Twinborn TiO_2-TiN heterostructures enabling smooth trapping-diffusion-conversion of polysulfides towards ultralong life lithium-sulfur batteries. *Energy. Environ. Sci.* **2017**, *10*, 1694-703. DOI
4. Sun, Y.; Wang, J.; Shang, T.; et al. Counting d-orbital vacancies of transition-metal catalysts for the sulfur reduction reaction. *Angew. Chem. Int. Ed.* **2023**, *62*, e202306791. DOI
5. Peng, L.; Shang, T.; Han, J.; et al. Nonpoisoned metal catalysts enabled by concave carbon confinement for durable sulfur conversion in batteries. *Energy. Environ. Sci.* **2026**, *19*, 982-94. DOI
6. Hua, W.; Shang, T.; Li, H.; et al. Optimizing the p charge of S in p-block metal sulfides for sulfur reduction electrocatalysis. *Nat. Catal.* **2023**, *6*, 174-84. DOI
7. Geng, C.; Lei, Y.; Shi, J.; et al. Ionic liquids anchored on carbon synchronize ion-electron transport in liquid- and solid-state sulfur batteries. *ACS. Energy. Lett.* **2025**, *10*, 5956-64. DOI
8. Liu, R.; Wei, Z.; Peng, L.; et al. Establishing reaction networks in the 16-electron sulfur reduction reaction. *Nature* **2024**, *626*, 98-104. DOI
9. Peng, L.; Geng, C.; He, Y.; et al. Surface charge-modulated electric-double-layer structure on Pt catalyst for efficient and durable sulfur reaction in Li-S batteries. *Angew. Chem. Int. Ed.* **2026**, *65*, e23287. DOI
10. Hu, Z.; Geng, C.; Shi, J.; et al. Breaking Li^+ diffusion limits in practical Li-S batteries via electrolyte-dispersible Li^+-reservoir catalysts. *J. Am. Chem. Soc.* **2025**, *147*, 41924-33. DOI
11. Yu, T.; Xiao, R.; Tang, P.; et al. Breaking insulating barriers in solid-phase conversion reactions with dual-atom catalysts for high-energy lithium batteries. *Nat. Catal.* **2026**, *9*, 460-70. DOI
12. Wu, Z.; Liu, M.; He, W.; et al. Unveiling the autocatalytic growth of Li_2S crystals at the solid-liquid interface in lithium-sulfur batteries. *Nat. Commun.* **2024**, *15*, 9535. DOI PubMed PMC
13. Bonilla, Á.; Gentile, A.; Ferrara, C.; et al. Dual role of $Ti_3C_2T_x$ MXene in Li-S batteries: cathode additive and separator modifier for enhanced performance. *Adv. Funct. Mater.* **2026**, *36*, e19742. DOI
14. Chen, X.; Jiang, H.; Liu, J.; et al. Covalent organic frameworks and their derivatives for applications in high-performance lithium-sulfur batteries. *Adv. Funct. Mater.* **2025**, *35*, 2421697. DOI
15. Jiang, Y.; Liao, Y.; Yu, J.; et al. Multi-effect ionic liquid additives achieve high cycle stability lithium-sulfur batteries by constructing an electrostatic shielding layer and eliminating 'dead sulfur'. *Adv. Funct. Mater.* **2025**, *35*, 2500077. DOI
16. Peng, L.; Han, J.; Cao, Y.; et al. Metal-halide gelated MXene and its use as a bifunctional sulfur host stabilizing both cathode and anode for practical lithium-sulfur batteries. *Adv. Funct. Mater.* **2024**, *34*, 2310508. DOI
17. Jiang, Q.; Xu, H.; Ye, X.; et al. Breaking the rate limiting barrier in lithium||sulfur batteries via spin state engineering. *Nat. Commun.* **2026**, *17*, 4466. DOI PubMed PMC
18. Dong, Y.; Cai, D.; Li, T.; et al. Sulfur reduction catalyst design inspired by elemental periodic expansion concept for lithium-sulfur batteries. *ACS. Nano.* **2022**, *16*, 6414-25. DOI
19. Jiang, M.; Shi, J.; Wang, J.; et al. Optimizing f-d hybridization descriptor in rare-earth oxides for efficient sulfur catalysis in all solid-state lithium-sulfur batteries. *Adv. Mater.* **2026**, *38*, e20011. DOI
20. Li, S.; Yang, H.; Tong, H.; et al. Orbital-tailoring strategy via dual-defect engineering in P-$FeTe_{2-x}$@NC synergizes polysulfide adsorption-conversion for lithium-sulfur batteries. *Adv. Mater.* **2025**, *37*, e11910. DOI
21. Hua, W.; Li, H.; Hu, Z.; et al. Phase engineering of 2D telluride crystals for sulfur catalysis in batteries. *Adv. Energy. Mater.* **2026**, *16*, 2501963. DOI
22. Gong, Q.; Yang, D.; Yang, H.; et al. Cobalt ditelluride meets tellurium vacancy: an efficient catalyst as a multifunctional polysulfide mediator toward robust lithium-sulfur batteries. *ACS. Nano.* **2024**, *18*, 28382-93. DOI

23. Yang, Z.; Yan, R.; Han, J.; et al. Oxygen bridges of $CoTe_2$/Co-O-NC enhancing adsorption-catalysis of polysulfide for stable lithium-sulfur batteries. *Adv. Funct. Mater.* **2025**, *35*, 2417834. DOI
24. Li, Q.; Liang, Z.; Huang, Y.; et al. Tailoring self-catalytic N-Co bonds into heterostructure architectures: deciphering polytellurides conversion mechanism toward ultralong-lifespan potassium ion storage. *Adv. Mater.* **2025**, *37*, e2502894. DOI
25. Zhu, Y.; Wang, M.; Ci, H.; Ding, Y.; Gao, X.; Sun, J. Decorating vertically oriented graphene arrays with Co-doped $NiTe_2$ toward Al-current-collector-free Li-S batteries. *Renewables* **2023**, *1*, 582-9. DOI
26. Bi, W.; Li, C.; Yang, D.; et al. MOF-derived ultrathin carbon nanosheets integrated with telluride nanoparticles: synergistic polysulfide adsorption and catalytic sites for enhanced sulfur redox reactions. *Energy. Environ. Sci.* **2025**, *18*, 1929-40. DOI
27. Shen, Z.; Jin, X.; Tian, J.; et al. Cation-doped ZnS catalysts for polysulfide conversion in lithium-sulfur batteries. *Nat. Catal.* **2022**, *5*, 555-63. DOI
28. He, C.; Yu, S.; Gao, X.; et al. Synergistic dual-gradient architecture and vacancy-engineered catalytic interfaces via p-band modulation for high-reversibility lithium-sulfur batteries. *Adv. Funct. Mater.* **2026**, *36*, e13418. DOI
29. Wang, W.; Wang, X.; Yang, H.; et al. Design rules for anion-doped catalysts revealed by p-p-s orbital coupling in Li-S chemistry. *Nat. Commun.* **2025**, *16*, 10895. DOI PubMed PMC
30. Hu, Z.; Geng, C.; Shi, J.; et al. In situ welding ionic conductive breakpoints for highly reversible all-solid-state lithium-sulfur batteries. *J. Am. Chem. Soc.* **2024**, *146*, 34023-32. DOI
31. Li, Q.; Xie, C.; Jiang, X.; et al. Catalytic solder fuses solid-solid interfaces for all-solid-state lithium-sulfur batteries. *Adv. Mater.* **2025**, *37*, e2507308. DOI
32. Yang, J. L.; Xu, H.; Xiao, T.; et al. High-dimensional strain unlocks fast polysulfide redox kinetics for lithium-sulfur batteries. *Nat. Commun.* **2025**, *16*, 8910. DOI PubMed PMC
33. Deelen TW, Hernández Mejía C, de Jong KP. Control of metal-support interactions in heterogeneous catalysts to enhance activity and selectivity. *Nat. Catal.* **2019**, *2*, 955-70. DOI
34. Lao, Z.; Han, Z.; Ma, J.; et al. Band structure engineering and orbital orientation control constructing dual active sites for efficient sulfur redox reaction. *Adv. Mater.* **2024**, *36*, e2309024. DOI
35. Wang, Y.; Liu, D.; Wang, H.; et al. Unified electronic-geometric descriptor deciphers peroxymonosulfate activation using Fe-based dual-atom catalysts. *Nat. Commun.* **2025**, *16*, 10491. DOI PubMed PMC
36. Wang, W.; Wang, X.; Shan, J.; et al. Atomic-level design rules of metal-cation-doped catalysts: manipulating electron affinity/ionic radius of doped cations for accelerating sulfur redox kinetics in Li-S batteries. *Energy. Environ. Sci.* **2023**, *16*, 2669-83. DOI
37. Yi, M.; Lv, S.; Chu, L.; et al. Ionic-liquid-assisted synthesis of NiTe/CoTe heterostructure with Te vacancies in N, P, and F Co-doped hollow carbon nanorods for efficient alkaline hydrogen evolution and high-performance flexible supercapacitors. *Rare. Metals.* **2026**, *45*, e70118. DOI
38. Wu, X.; Xie, R.; Cai, D.; et al. Engineering defect-rich bimetallic telluride with dense heterointerfaces for high-performance lithium-sulfur batteries. *Adv. Funct. Mater.* **2024**, *34*, 2315012. DOI
39. Li, P.; Luo, Z.; Chen, Z.; et al. Hyaluronic acid with double helix ion channels for efficient electrolyte retention and polysulfide regulation in lean-electrolyte lithium-sulfur batteries. *Adv. Mater.* **2025**, *37*, e11272. DOI
40. Jiang, X.; Qu, W.; Ye, R.; et al. A band-matching descriptor breaks scaling relations for sulfur electrocatalysts. *J. Am. Chem. Soc.* **2026**, *148*, 19048-60. DOI
41. Na, F.; Li, X.; Wang, J.; et al. Immobilizing single atom on high-entropy oxides as separator regulators for catalyzing low-temperature lithium-sulfur battery. *Energy. Storage. Mater.* **2025**, *78*, 104228. DOI
42. Mao, Y.; Zhang, Y.; Su, M.; et al. Synergetic insights into Nb single atoms and lithiophilic support for high-efficiency sulfur catalysis in Li-S batteries. *Energy. Environ. Sci.* **2025**, *18*, 8631-44. DOI
43. Huang, Y.; Li, J.; Zhang, Y.; et al. Energizing robust sulfur/lithium electrochemistry via nanoscale-asymmetric-size synergism. *J. Am. Chem. Soc.* **2025**, *147*, 4752-65. DOI
44. Han, Z.; Gao, R.; Wang, T.; et al. Machine-learning-assisted design of a binary descriptor to decipher electronic and structural effects on sulfur reduction kinetics. *Nat. Catal.* **2023**, *6*, 1073-86. DOI
45. Zhao, Y.; Geng, C.; Wang, L.; et al. Engineering catalytic defects via molecular imprinting for high energy Li-S pouch cells. *Natl. Sci. Rev.* **2024**, *11*, nwae190. DOI PubMed PMC
46. Zhu, X.; Wang, W.; Dou, W.; et al. Directional catalysis of sulfur at highly ordered triple-phase interfaces in all-solid-state lithium-sulfur batteries. *Adv. Mater.* **2026**, *38*, e22483. DOI
47. Zhang, Y.; Li, X.; Wang, Y.; et al. Edge-delocalized electron effect on self-expediating desolvation kinetics for low-temperature Li-S batteries. *Adv. Funct. Mater.* **2025**, *35*, 2508225. DOI
48. Cheng, Z.; Wu, P.; Dong, W. X.; et al. Biomimetic gradient-porous carbon enables sustainable high-loading lithium-sulfur batteries by regulating polysulfide chemistry. *Angew. Chem. Int. Ed.* **2026**, *65*, e5836599. DOI

49. Li, Z.; Liu, R.; Chen, Q.; Wen, M.; Huang, X.; Yue, Q. Two-dimensional mesoporous tungsten oxynitride/carbon nanosheets: enabling high-performance lithium-sulfur batteries. *Angew. Chem. Int. Ed.* **2026**, *65*, e9899225. DOI
50. Zhao, W.; Mao, Y.; Zhang, W.; et al. Nanoheterocrystal catalysts designed by multiple reactivity descriptors for accelerated redox kinetics in Li-S batteries. *ACS. Nano.* **2026**, *20*, 8659-70. DOI
51. Zhu, R.; Wu, Z.; He, C.; et al. Electronegative Co-WO_2 interface with Li^+ pump effects for efficient polysulfide conversion in high-performance Li-sulfur batteries. *ACS. Nano.* **2025**, *19*, 23479-89. DOI
52. Tian, J.; Yang, Z.; Xiao, T.; et al. Oxygen bridge-induced spin-state engineering enables solvation-barrier-free sulfur redox kinetics in lithium-sulfur batteries. *Angew. Chem. Int. Ed.* **2026**, , e4944842. DOI
53. Kong, Y.; Wang, L.; Mamoor, M.; et al. Co/Mon invigorated bilateral kinetics modulation for advanced lithium-sulfur batteries. *Adv. Mater.* **2024**, *36*, e2310143. DOI
54. He, Y.; Xiong, D.; Chen, M.; et al. Modulating ion-dipole and dipole-dipole interactions for stable wide-temperature-range lithium–sulfur batteries enabled by quantum-dot catalysts. *Angew. Chem. Int. Ed.* **2025**, *137*, e202512168. DOI
55. Wang, B.; Wang, L.; Ding, D.; et al. Zinc-assisted cobalt ditelluride polyhedra inducing lattice strain to endow efficient adsorption-catalysis for high-energy lithium-sulfur batteries. *Adv. Mater.* **2022**, *34*, e2204403. DOI
56. Liu, L.; Cui, H.; Shen, J.; et al. Synergistic interface engineering of heterojunction and oxygen vacancies in multiphase cobalt oxide/graphene composite host for high-performance lithium-sulfur batteries. *Adv. Energy. Mater.* **2026**, *16*, e06549. DOI
57. Deng, D. R.; Xiong, H. J.; Luo, Y. L.; et al. Accelerating the rate-determining steps of sulfur conversion reaction for lithium-sulfur batteries working at an ultrawide temperature range. *Adv. Mater.* **2024**, *36*, e2406135. DOI
58. Lin, Y.; Wang, J.; Zhang, X.; et al. Single atom-particle tandem catalysis enables enhanced desolvation kinetics for low-temperature Li-S batteries. *Adv. Funct. Mater.* **2025**, *35*, 2501496. DOI
59. Zeng, Q.; Xu, L.; Li, G.; et al. Integrating sub-nano catalysts into metal-organic framework toward pore-confined polysulfides conversion in lithium-sulfur batteries. *Adv. Funct. Mater.* **2023**, *33*, 2304619. DOI
60. Soria-fernández, A.; Castillo, J.; Robles-fernandez, A.; Gadea, S.; Santiago, A.; Carriazo, D. Integrated sparingly solvating electrolyte-catalyst strategies to unlock lithium-sulfur battery viability: a perspective. *Batter. Supercaps.* **2026**, *9*, e202500313. DOI